Impact of catalyst support morphology on 3D electrode structure and polymer electrolyte membrane fuel cell performance

Peter Benedikt[1] | **Daniela Stoeckel**[2,3] | **Torsten Scherer**[4] | **Christian Kuebel**[4] | **Christina Roth**[5] | **Julia Melke**[6,7] (ORCID)

[1] Department of Materials and Geosciences, Technical University Darmstadt, Darmstadt, Germany

[2] Institute of Physical Chemistry, Justus-Liebig-Universität Gießen, Gießen, Germany

[3] Department of Chemistry, Philipps-Universität Marburg, Marburg, Germany

[4] Institute of Nanotechnology & Karlsruhe Nano Micro Facility, Karlsruhe Institute of Technology, Eggenstein-Leopoldshafen, Germany

[5] Electrochemical Process Engineering, University of Bayreuth, Bayreuth, Germany

[6] Department for Applied Electrochemistry, Fraunhofer Institute for Chemical Technology, Pfinztal, Germany

[7] Institute of Inorganic and Analytical Chemistry, Albert-Ludwigs-Universität Freiburg, Freiburg, Germany

Correspondence
Julia Melke, Fraunhofer Institute for Chemical Technology, Pfinztal, Germany.
Email: julia.melke@ict.fraunhofer.de

Funding information
German Science Foundation DFG, Grant/Award Number: Ro2454/10-1

Abstract

Porous carbon-based electrodes are frequently applied in electrochemical energy technologies, for instance in fuel cells and redox flow batteries. In previous work, we observed that the final structure of a fuel cell electrode is dominated by both the morphology of the support material and its processing into a 3D porous structure. Herein, the impact of catalyst support morphology on the performance of polymer electrolyte membrane fuel cells was studied comparing carbon-supported platinum catalysts only differing in the shape of the carbon support material with otherwise similar features. Carbon-supported Pt catalysts were obtained by carbonization of polyaniline (PANI) in long fibrous, short fibrous, and granular shape. The chemical identity of the PANI precursors was demonstrated by FTIR spectroscopy and elemental analysis (EA). The final carbon-supported platinum catalysts were characterized by EA, Raman spectroscopy, XRD, and TEM exhibiting similar degree of carbonization, nanoparticle size, and nanoparticle dispersion. The effect of support morphology and the resulting differences in the 3D structure of the porous electrode were investigated by focused ion beam-scanning electron microscopy slice and view technique and correlated to their fuel cell performance.

KEYWORDS

3D reconstruction, FIB-SEM, fuel cells, N-doped carbon, PEMFC, polyaniline, support morphology

1 | INTRODUCTION

In polymer electrolyte membrane (PEM) fuel cells, supported platinum nanoparticle catalysts are widely employed, in order to reduce the amount of noble metal required and thereby reduce the cost of the device. Carbon is the support material of choice, as it is cheap, inert, and provides a good dispersion and narrow size distribution of the catalytically active noble metal phase. Furthermore, it is sufficiently electron-conducting and stable at the high

potentials in acidic electrolytes. Such supported catalysts containing additionally a proton-conducting ionomer are mixed to a viscous ink and then processed into a porous 3D structure, for example, by airbrushing. After drying, the obtained porous catalyst layer constitutes the electrode, at which either the oxygen reduction reaction (ORR) or the hydrogen oxidation reaction (HOR) takes place. Depending on the electrode's porosity, pore connectivity, and the interdigitation of electron and proton-conducting pathways, the transport of educts and products (H^+, e^-, H_2, O_2, water) appears to be more or less hindered. This will lead to differences in mass transport and reaction kinetics at the electrodes significantly affecting the fuel cell performance.[1–5].

There are different ways to manufacture porous electrodes,[2] such as airbrushing,[6] electrospraying,[7] and sieve-printing,[6,8] but also electrospinning.[9,10] The ultimate goal of all fabrication strategies is to create a porous structure that allows for all transport processes to take place efficiently. Therefore, a balanced system of the micro (<2 nm), meso (2–50 nm), and macro pores (>50 nm) is required. Consequently, a lot of effort has been addressed to the development of fabrication techniques, which allows for significant control over the finally formed 3D architecture[3,8,10,11] but can still be scaled up at low cost. This is not an easy task, since most manufacturing techniques suffer from variances in catalyst distribution and loading, catalyst layer thickness, pore sizes, and pore size distribution as well as inhomogeneities in the catalytic layer originating from instabilities (e.g., nozzle blocking, slight changes in ink viscosity, etc.) during processing.

It has been shown previously that the 3D architecture of electrodes in electrochemical energy devices can be investigated in detail by the focused ion beam (FIB)-scanning electron microscopy (SEM) slice&view technique and subsequent 3D reconstruction.[12,13,14,15] This technique has for instance been used to study degradation phenomena in PEM fuel cell electrodes,[16,17] as well as the impact of various electrode fabrication processes on the resulting 3D electrode structure.[18] Early work by Ettingshausen et al.[19] and Litster et al.[2] already indicated the important role of the support material's shape for the formation of the porous structure of the catalytic layer in fuel cells. They found that the electrode's 3D architecture is largely dominated by the morphology of the support material.

With the above in mind, the first idea to systematically tune the structure of the porous electrode may be to vary the shape of the used support materials. However, this is not as easy as it seems, because on the one hand, surface functionalization and microporosity of the carbon support impact ionomer distribution,[20,21] and Pt nanoparti-

cle size distribution and dispersion[21,22] thereby influencing the electrochemical activity of the carbon-supported metal catalyst. On the other hand, also the processing of the catalyst on to the polymer electrolyte membrane is affected by carbon surface functionalization. For example, for Pt supported on carbon nanotubes the dispersion of catalysts within the ink, which had been spray-coated on the membrane, depends on the surface functionalization of the CNTs.[23] In turn the properties and composition of the catalyst suspension/paste and the processing conditions also determine the final electrode structure.[15] Hence, in order to solely study the effect of the support morphology on the fully processed electrode structure, we chose an approach, in which chemically identical starting materials differing only in shape were synthesized and transferred into carbons with largely identical features. In the present work, polyaniline (PANI) was chosen as starting material, as it is a well-established polymer that is facile to synthesize in different morphologies, but with the same chemical properties.[24] Employing different acids in the synthesis protocol led to different shapes, which can be controlled from long fibers to short fibers to granular shape. Carbonization at temperatures up to 1000°C in N_2 yields N-doped carbon supports, while the support shape is maintained throughout the heat-treatment[25,26]. As a uniform decoration of the carbonized PANI with Pt nanoparticles is difficult, we decorated PANI with platinum before its carbonization resulting in an enhanced stability of the nanoparticles. This peculiar behavior has already been demonstrated in our previous study,[27] and was identified to result from the strong Pt-N interactions.[28] Using SEM and FIB slice&view techniques in a large volume combined with a detailed pore analysis, we demonstrate herein the significant effect of support morphology on the electrode structure and thus fuel cell performance.

2 | EXPERIMENTAL SECTION

2.1 | Synthesis of platinum on carbon supports with different morphologies

PANI powders with particles of three different morphologies were prepared using modified oxidative polymerization reactions known from the literature.[24,26] Aniline (450 μl) and ammoniumperoxodisulphate (APS; 1428 g) were dissolved in 50 ml acid each. To achieve the different morphologies, either 0.4 M acetic acid, 1 M, or 0.1 M sulfuric acid was used in order to obtain long PANI fibers, short PANI fiber, or granules of PANI, respectively. Under rapid stirring, the APS solution was poured into the aniline solution, after that the reaction mixture was kept untouched

for 24 h. The resulting PANI material was filtered, washed with ethanol and water, and stored in wet conditions until further use.

To obtain 20 wt% Pt on carbonized PANI, a Pt/PANI loading of roughly 11 wt% was prepared in the starting material using a formic acid method proposed by Guo et al.[29] before carbonization, since it is known from the literature, that PANI will lose roughly 50% of its weight under these heat-treatment conditions.[25] A mass corresponding to 400 mg dry PANI of each morphology was dispersed in 30 ml ultrapure water (MilliQ 18.2 MΩ @25°C) using an ultra turrax homogenizer. When a good dispersion was achieved, 125 mg H_2PtCl_6 (40 wt% Pt) were added and stirring was continued for two more hours to allow for good contact of platinum ions and PANI.[30] Then 3 ml of HCOOH were added dropwise while stirring and the mixture was stored without stirring for 24 h to reduce the platinum precursor completely. After filtration, the precipitates were dried in a vacuum at room temperature to minimize agglomeration.

The carbonization treatment was carried out in a tube furnace under nitrogen flow. The samples were placed in an alumina crucible and heated with a ramp of 1°C/min up to 750°C. After holding the sample at the final temperature for 90 min, the furnace was switched off and samples cooled down to room temperature before removing.

2.2 | Physico-chemical characterization of PANI precursors and resulting Pt catalysts powders

Fourier transform infrared (FTIR) spectroscopy was applied to ensure the chemical identity of the as-prepared PANI. Small amounts of the dried PANI powders were ground in a mortar together with 150 mg KBr until the powder turned to a pale green. A pellet with 13 mm diameter was pressed using a hydraulic hand press with 10 t pressure for 3 min. For each pellet 64 scans were measured in the range from 4000 cm^{-1} to 400 cm^{-1} with a resolution of 1 cm^{-1} using a Vertex 70 (Bruker).

The elemental composition of the materials before and after carbonization was determined with a Vario Micro Cube™ elementary analysis system, which can detect the elements C, H, N, and S. Each result is the average of two individual measurements using roughly 3 mg of the starting material.

Surface area measurements were obtained by N_2 sorption measurements using a Quantachrome NovaWin from NOVA instruments. Samples were dried overnight in a vacuum at 80°C, weighed, and then dosed with N_2 (molecular cross-section = 0.1620 nm^2) at 77.3 K.

X-ray diffraction (XRD) measurements were carried out with an STOE STADI-P diffractometer in transmission geometry using germanium monochromized Mo K$_{\alpha1}$ radiation ($\lambda = 0.71069$ Å). To determine the average crystallite size of the platinum particles, Rietveld refinement using the FULLPROF software package was performed.[31]

Transmission electron microscopy (TEM) was performed at a Philips CM20 und an acceleration voltage of 200 kV. For all samples, a small amount of powder was dispersed in ethanol by ultrasonication and one drop was placed on a TEM grid. The platinum nanoparticles size distribution was determined by analyzing at least 200 particles for each sample.

Raman measurements were performed at a Senterra Microscope (Bruker) using a laser wavelength of 532 nm with a spectral resolution of 4 cm^{-2}. In order to reduce beam damage at the sample, the laser power was reduced to 1 mW. For each sample up to 20 spectra were measured at different positions and averaged.

2.3 | Preparation of catalyst coated membranes

All catalyst coated membranes (CCMs) were prepared in the same way. A Nafion 117® membrane was fixed standing upright in a heated (100°C) spraying mask with vacuum from the backside. The mask allows to prepare a 5×5 cm^2 and a 5×1 cm^2 electrode sample at the same time. The 5×5 cm^2 CCM was operated as a fuel cell and the 5×1 cm^2 CCM was used for the 3D structure investigations. First, the anode consisting of 200 mg commercial Pt on carbon black (Alfa Aesar, platinum nominally 20% on carbon black) dispersed in 9 ml MilliQ water, 1 ml Nafion® solution (5 wt% in lower aliphatic alcohols and water, D520, DuPont) and 20 ml isopropanol was sprayed using a modified airbrushing method. For cathode preparation, a modified fast spraying method,[32] derived from the layer-by-layer (LbL) method[33] was used. Therefore, two different solutions were prepared: The first solution contained 200 mg of the as prepared catalyst dispersed in ethanol-water (1:1) with pH 2.6, the second solution contained 1 ml Nafion® solution dispersed in 49 ml ethanol–water mixture (1:1). Both solutions were sprayed alternately onto the other side of the Nafion membrane, mounted onto the heated vacuum plate standing upright. The heating leads to an immediate drying of the suspensions that allows to control the thickness of the resulting layers.

The platinum loading of the cathodes was determined by thermogravimetric analysis (TGA) using a Netzsch STA 449C Jupiter under synthetic air (Linde, 80% N_2, 20% O_2) with a heating rate of 5°C min^{-1} in a range from 30 to 1000°C.

2.4 | Fuel cell measurements

The prepared CCMs were tested in a homemade test bench using a Quickconnect® fixture at 5 bar. The CCM was sandwiched between two Freudenberg I3 GDL (Freudenberg, Weinheim) and two graphitic flow fields with lamellar four channel structure. The cell temperature was set to 70°C, hydrogen with a flow rate of 150 ml/min, and oxygen with 80 ml/min were both humidified using bubbler humidifiers (anode: 80°C; cathode: 85°C) before being fed into the fuel cell.

For CO stripping measurements in the fuel cell setup, the cathode was flushed with dry nitrogen for 1 h before the load was replaced by a potentiostat (Gamry Reference 600®). The anode was fed with hydrogen and used as a counter- and reference electrode at the same time. Subsequently, CO was added into the N_2 stream for 15 min while the potential of the electrode was held at 0.1 V versus the reference hydrogen electrode (RHE). After the CO was adsorbed to the catalyst surface, the electrode compartment was further flushed for 45 min with N_2 with potential retained at 0.1 V versus RHE in order to remove CO in the gas phase. Afterward, the CO is stripped off by cycling the potential up to 1.25 V versus RHE using a scan rate of 20 mV/s. The CO stripping cycle is followed by five cycles in the range of 1.25 V versus RHE to 0.05 V versus RHE. The electrochemically active surface area (ECSA) was calculated from the CO stripping peak by integrating the charge due to CO oxidation Q_{co} by the following equation:

$$ECSA \ \left[cm^2 g_{Pt}^{-1}\right] = \frac{Q_{co}}{2 \cdot 210 mC \ cm^{-2}} \cdot \frac{1}{m_{Pt}} \quad (1)$$

2.5 | Investigations of 3D electrode structures

SEM (FEI Quanta 200 FEF operated at 20 kV acceleration voltage) was used to investigate the electrode thickness of the prepared CCMs. Therefore, the $5 \times 1 \ cm^2$ CCMs were embedded in Araldit® (polymerization at 60°C for 16 h) and a cross section was prepared using an ultramicrotome (Reichert-Jung Ultracut E ultramicrotome, DKK diamond knife).

FIB-SEM slice&view 3D reconstructions were performed on an FEI Strata 400 S system equipped with a Sidewinder™ ion column using the Auto slice&view package. To minimize surface damage, a platinum protective layer with a thickness of about 1 μm was deposited on the CCM before milling. Then a standard cross section (Figure 1a) was milled to allow electron beam imaging of the area of interest (Figure 1b). During slice and view operation, 400 FIB cuts were made with a thickness of 20 nm

each using a 30 kV Ga⁺-ion beam. For each cut, the corresponding area was imaged using the SEM at 5 kV. Figure 1c,d displays the last FIB and the last SEM image, respectively, which were captured. Comparing Figure 1a,b the volume that was cut during the procedure can be estimated.

The FIB-SEM slice&view image stack was aligned using IMOD V4.7[33] by cross-correlation of an area next to the region of interest (ROI) that did not change during data acquisition. Afterward, the y-position of each slice was compensated for the inclined viewing angle of the SEM. Finally, the ROI was cropped, and combined into a stack of 400 8-bit grayscale images recorded at axial intervals of 20 nm. After the alignment, a representative area of roughly $4 \times 4 \times 4 \ \mu m^3$ was chosen and binarized manually using Amira 5.4 (FEI Company) taking care that only the foreground structure was selected for the pore edge. The 3D visualization and graphical outputs were generated using Amira. In order to evaluate the reconstructed pore space statistically, a chord length distribution (CLD) was calculated from the binarized data sets. An in-house software developed in Visual Studio C# 2008 (Microsoft Corporation, Redmond, WA) was used for this. Random points were generated in the void area of the image stack and from each point, 32 vectors were projected in angularly equispaced directions as described elsewhere.[34] The resulting chords are the sum of the absolute lengths of an opposed pair of vectors, describing a straight distance between two interfaces (pore wall-to-pore wall). Chords that projected out of the image were discarded. For each CLD 10^6 chords were collected and the results were displayed in a histogram using a binning size of 50 nm.

3 | RESULTS AND DISCUSSION

3.1 | Chemical identity: Support and catalyst characterization

In a first step, the three different catalysts (Pt-on-long-fibers, Pt-on-short-fibers, and Pt-on-granules) were characterized in-depth with respect to the chemical identity of the different PANI support precursors and the final features of the carbon support and Pt nanoparticles, such as particle size and distribution. First, FTIR absorption spectra of the three different protonated PANI precursors were measured showing nearly the same characteristics (Figure 2a). The characteristic absorption bands present in all samples are quinonoid ring stretching at 1585 cm⁻¹, benzenoid ring stretching at 1497 cm⁻¹, C-H stretching at 1300 cm⁻¹, C-N⁺ stretching at 1244 cm⁻¹, benzoid-NH stretching at 1150 cm⁻¹, and aromatic C-H out of plain vibration at 823 cm⁻¹ in agreement with previous investi-
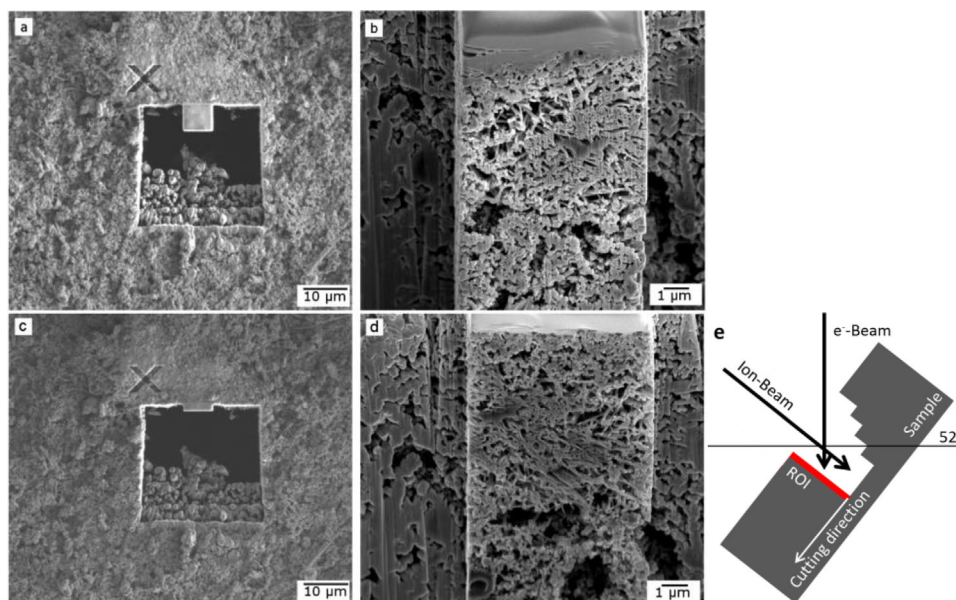
FIGURE 1   Representative images from the FIB-SEM imaging. (a) FIB image after pre-milling, the freestanding cubic area that has been pre-milled will be cut into thin slices during the FIB-SEM process, (b) SEM image corresponding to FIB sections perpendicular to the surface, while the electron beam is arranged at an angle of 52°, (c) FIB-image after 400 slice and view cycles, (d) SEM image corresponding to (c). Figure part (e) shows a schematic of the FIB alignment
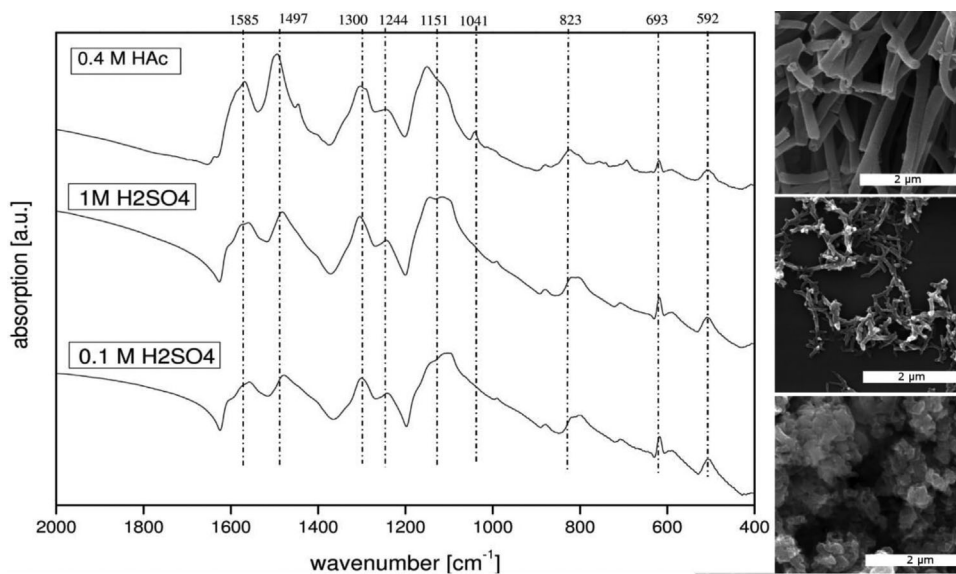
FIGURE 2   IR spectra (a) of the three PANI samples with different morphologies. TEM images of the different PANI morphologies: Long fibers were obtained via the synthesis in 0.4 M acetic acid (b), short fibers in 1 M sulfuric acid (c), and granular material in 0.1 M sulfuric acid (d)

gations of PANI.[30,24] Additional absorption bands arise at 1440 cm^{-1}, 1041 cm^{-1}, 693 cm^{-1}, and 592 cm^{-1} that can be assigned to hydrogen sulfate and/or sulfate counterions.[26] At a first glance it might surprise that these peaks are more pronounced in the sample prepared without sulfuric acid. However, sulfuric acid is produced as a by-product during the polymerization of aniline in such amounts that it is sufficient to fully protonate the PANI.[24] Small shifts in the bands around 1497 cm^{-1} and 823 cm^{-1} as well as a difference in height at 1585 cm^{-1} were observed. These variations are due to some discrepancies in the amino groups in the ring structures, like anionic or cationic

6 of 13 **Electrochemical Science Advances**
RESEARCH ARTICLE
doi.org/10.1002/elsa.202100121

Chemistry
Europe
European Chemical
Societies Publishing

TABLE 1 Elemental analysis, XRD and BET measurements of PANI precursor and the resulting Pt catalysts after carbonization

	PANI precursor			PANI based Pt/C catalyst		
	Long	Short	Granular	Long	Short	Granular
C [wt%]	57.8	56.8	54.9	59.4	50.7	53.9
N [wt%]	10.9	10.5	10.1	8.2	7.3	5.9
S [wt%]	5.07	4.71	5.75	0.4	0.8	0.5
H[wt%]	4.8	4.9	4.9	1.5	1.9	1.3
C/N	5.3	5.4	5.4	7.2	6.9	10.2
d-Pt [nm] (XRD)	n.a.	n.a.	n.a.	3.2	3.3	3.1
d-Pt [nm] (TEM)	n.a.	n.a.	n.a.	2.4 ± 1.2	2.5 ± 1.12	2.7 ± 1.0
BET [$m^2/g_{catalyst}$]	30	39	36	79	98	112

amino groups, which led to the different morphology during formation, but do not affect the chemical behavior.[24]

In good agreement with the FTIR measurements, elemental analysis (Table 1) of the three morphologically different PANI precursors also obtained almost identical results. All PANI precursors contain around 10.5 wt% N and 5 wt% S of residual sulfuric acid. Pt deposition and carbonization at 750°C show that the number of N-groups decreases as found by elemental analysis (Table 1). For the PANI precursors, C:N was determined to be around 5.4:1 and for the carbonized materials, C:N changed to around 7:1. TEM images of the resulting Pt catalysts reveal a homogenous Pt nanoparticle distribution (Figure 3a–c) as a result of the strong Pt-N interactions, as already shown previously.[28]

TEM images at higher magnification revealed the presence of small platinum nanoparticles with a bimodal particle size distribution. The smaller particle size distributions are similar in particle size and homogeneity and with rather uniform distances between particles when comparing the microscopic images for the three differently shaped support materials. Calculating the mean diameter of all particles in an arbitrary region, we found 2.4 ± 1.2 nm for the Pt particles on the long fibers, 2.5 ± 1.1 nm on the short fibers, and 2.7 ± 1.0 nm on the granular material. Analysis of their XRD patterns by Rietveld Refinement reveals crystallite sizes in the range of 3 nm for all three catalysts. However, the discrepancy between data and the fit results indicates the presence of a bimodal particle size distribution. The reflections exhibit a peculiar reflection profile, which can be explained by overlaying reflections of a large size and a small size crystallite fraction. However, the overall discrepancy between data and fit is too small to properly include a bimodal crystallite size distribution. Thus, the mean crystallite size obtained by Rietveld Refinement and assuming a monomodal crystallite size distribution is

slightly too large, which is in agreement with the smaller particle sizes found by TEM analysis compared to the crystallite sizes found by XRD. In summary, particle size distribution and particle dispersion on the differently shaped carbon supports have been found to be nearly identical for all three catalysts.

Furthermore, Raman measurements (Figure 4) were performed in order to investigate the progress in graphitization for the different materials, when being transferred from the PANI precursor to the carbon material. For all three catalysts, identical D and G bands were found by Raman microscopy indicating identical graphitization degrees. However, the in-plane crystallite length as proposed by Tuinstra-Koenig was not determined, because large amounts of sp^3 carbon are present in the specimens making a proper determination by Raman spectroscopy difficult.[35] Comparing the results to other PANI-based carbon materials,[36] which have been carbonized at a similar temperature, 700°C, these exhibit a similar Raman spectrum and C:N ratio with 8.8:1. As they observed crystallite domains with sizes of around 9 Å and an sp^2-C content of approximately 55%, a similar microstructure for the PANI-based catalysts in this study can be expected. Furthermore, N_2-sorption experiments for the three catalysts show similar surface areas. The BET surface areas were determined to be 78.7 m^2/g for the long fibers, 98.0 m^2/g for the short fibers, and 111.9 m^2/g for the granular support material, differing only slightly from sample to sample (Table 1). The values are in a range comparable to Vulcan XC72 and Pt supported on Vulcan XC72 (200 m^2/g and 50 m^2/g, respectively), which are applied as state-of-the-art electrocatalysts in PEMFC applications.[37]

Summarizing the above results, the measured characteristics are similar enough to describe the catalysts as almost identical with their main difference being the support morphology. Subsequently, the morphologically different cat-
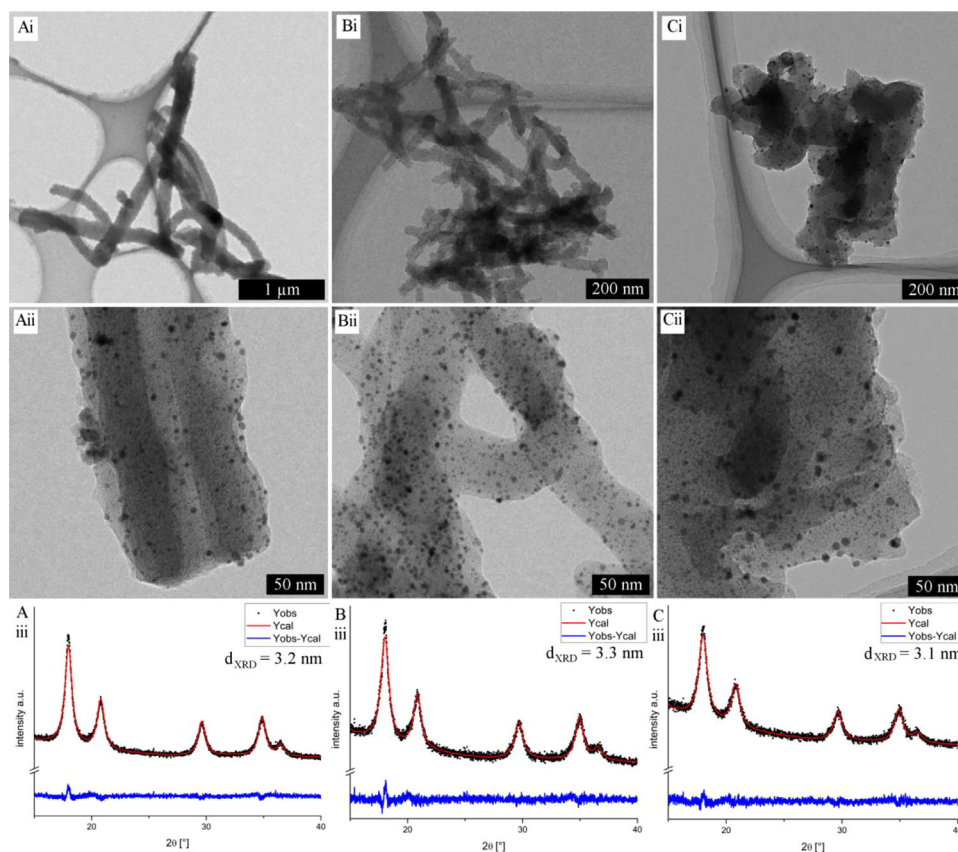
FIGURE 3 XRD and TEM of the three catalysts showing similar Pt particle size and distribution. A refers to PANI_750_long, B to PANI_750_short, and C to PANI_750_gran. i Overview, ii detailed images at the same magnification and iii corresponding diffraction patterns with Rietveld refinement
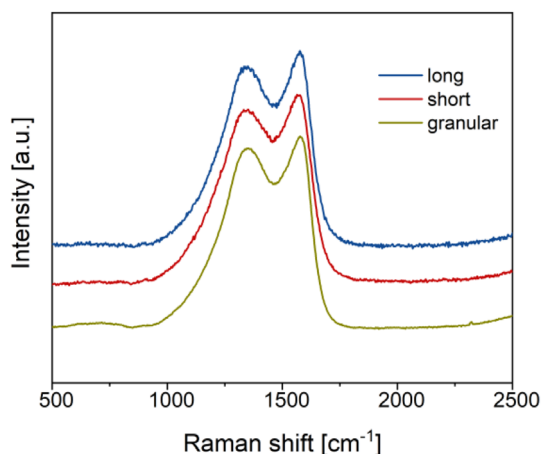

FIGURE 4 Raman spectra of the catalysts, PANI_750_long, PANI_750_short and PANI_750_gran

alysts were used to fabricate catalyst-coated membranes (CCM) by a layer-by-layer (LbL) spraying approach.[32] The catalysts were sprayed on one side of the membrane only, while for the opposite electrode always the same material, a commercial Pt/C catalyst, was used and processed using a routine airbrush procedure.

3.2 | Fuel cell performance

All three CCMs were tested as described in Section 2.5 in a single cell test bench using identical test conditions with the different catalyst morphologies operated as cathodes. Polarization curves were recorded automatically and power density curves were calculated on the basis of the polarization curves (Figure 5). The best performance was found for the CCM prepared using the carbon fiber catalyst CCM_{long}. It has to be noted that the maximum power density to the mass of Pt for this CCM_{long} is four times lower compared to a CCM prepared in the same way using a commercial Pt/C catalyst.[18] This result is partly due to the deposition of Pt nanoparticles onto the PANI before the carbonization treatment (as Pt nanoparticles might become buried within the carbon support and thus not accessible) leading to a low ECSA as found by rotating disk electrode measurements.[28] Nevertheless, as all PANI-based materials in these studies have been carbonized after Pt deposition a comparison between them is still meaningful. A summary of the characteristic values of the three CCMs in given in Table 2.
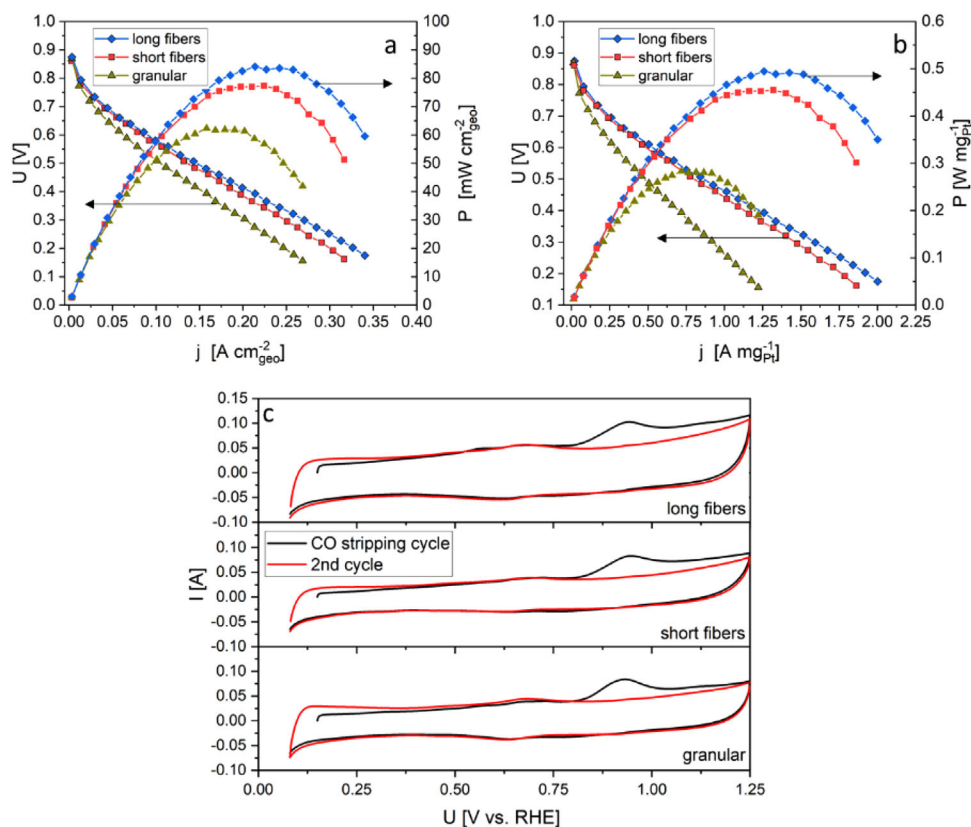
FIGURE 5 Polarization and power density curves related to the geometrical cell area (a) and the amount of Pt (b) of the CCMs employing three different support morphologies, PANI_750_long, PANI_750_short, and PANI_750_gran as cathode electrodes. CO-stripping curves of the different electrodes are presented in (c)

TABLE 2 Characteristic values for the three different CCMs

CCM with respective cathode morphologies	Pt loading	Electrode thickness	Maximum Power density	ECSA$_{CO}$	ECSA$_{CO}$
	[mg$_{Pt}$/cm$_{geo}^2$]	[μm]	[mW/mg$_{Pt}^1$]	[cm²]	[cm²/g]
Long	0.17 ± 0.02	20.6 ± 1.0	492	625	147
Short	0.17 ± 0.02	19.2 ± 1.1	455	450	106
Granular	0.22 ± 0.02	21.8 ± 1.9	283	345	62.5

All three polarization curves show nearly the same open circuit potential of roughly 870 mV, but the slope of the ohmic region shows clear differences. For CCM$_{gran}$, an ohmic resistance of 83.9 mΩ has been observed, which is higher than that for CCM$_{short}$ (73.5 mΩ) and CCM$_{long}$ (66.2 mΩ). The maximum power density P observed for the three samples follows the order: $P_{long, max} = 83.6$ mW/cm$_{geo}^2$, $P_{short, max} = 77.4$ mW/cm$_{geo}^2$, $P_{gran, max} = 62.3$ mW/cm$_{geo}^2$ (Figure 5a). Accounting for the amount of Pt loading at the cathode the maximum power density was found to be: $P_{long, max} = 492$ mW/mg$_{Pt}$, $P_{short, max} = 455$ mW/mg$_{Pt}$, and $P_{gran, max} = 283$ mW/mg$_{Pt}$ (Figure 5b). Interestingly, the lowest mass-related power

density has been found for the CCM with granular support morphologies exhibiting the largest Pt loading with 0.22 mg$_{Pt}$/cm$_{geo}^2$ compared to the other two cathode electrodes (short and long fiber) with 0.17 mg$_{Pt}$/cm$_{geo}^2$. CO-stripping (Figure 5c) of the different cathodes revealed also different electrochemically active surface areas with 147 cm²/g$_{Pt}$, 106 cm²/g$_{Pt}$, and 62.5 cm²/g$_{Pt}$ for long fiber, short fiber, and the granular-shaped catalysts. Thus, the accessibility of the Pt nanoparticles decreases with decreasing length of the fibers and is found to be the lowest for the granular catalyst in accordance with the cell performance. This difference in accessibilities despite the chemical identity of the catalyst materials with respect to carbon
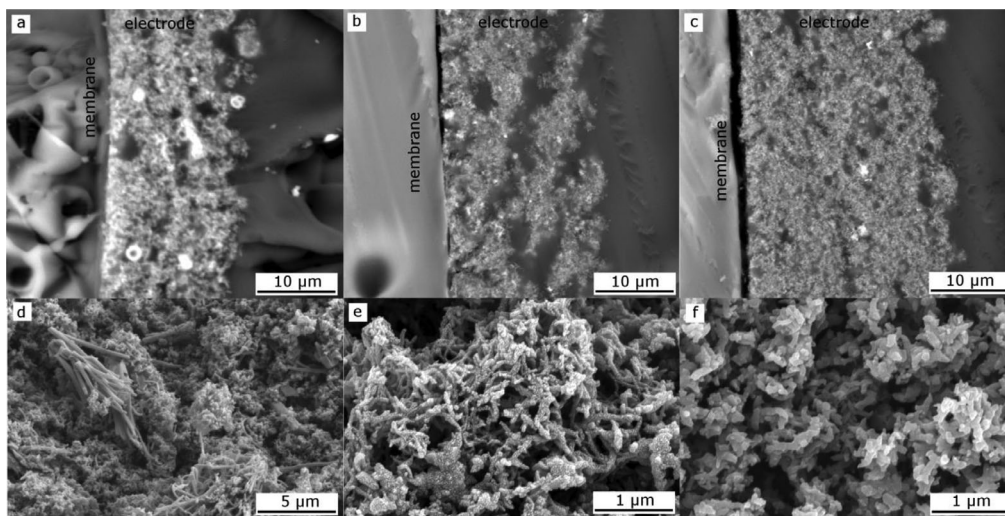
FIGURE 6 Cross sections (a-c) and surface views (d-f) of the CCMs. long (a+d), short (b+e), gran (c+f). The surface view of the long fibers (d) has a higher magnification so that the fibers become visible in their complete length. Besides the long fibers, there is a small amount of material (less than 50%) in other shapes, which is due to the synthesis

features, elemental composition, and Pt nanoparticle size indicates that the performance variations are caused by differences in the porous network architectures of the electrode rather than differences between the electrocatalysts. In the subsequent section, the electrode structures are further investigated to probe the morphology-performance correlation further.

3.3 │ 3D structure: SEM, FIB-SEM, and chord-length analysis

Before the detailed 3D investigation of the electrode structure, resin-embedded samples were investigated by SEM to determine the electrode thicknesses. The cross-sectional images are shown in Figure 6a–c. Top views of the electrode surfaces were used to get a first impression of the structure and porosity of the catalytic layers (Figure 6e,f). All three electrodes show a homogeneous thickness in the range of 20 μm (CCM$_{long}$: 20.6 $\pm$ 1.0 μm, CCM$_{short}$: 19.2 $\pm$ 1.1 μm, CCM$_{gran}$: 21.8 $\pm$ 1.9 μm). This thickness is in the range reported previously for multilayer electrodes using the same amount of catalyst and ionomer.[18] Due to the embedding in the resin, the structure of the electrodes was not visible in these cross-sections, but top views (Figure 6d–f) of the electrode surface revealed that the morphology of the support material is maintained also during and after electrode fabrication by the horizontal LbL process.

As the CCM fabricated with long and short fibers exhibits the largest similarity on Pt particle size and elemental composition, for both CCMs, a 3D reconstruction

based on FIB-SEM measurements was performed. The 3D reconstructions of CCM$_{long}$ and CCM$_{short}$ are shown in Figure 7a,b, respectively.

In both samples, the morphology of the support material is clearly visible. For the sample prepared by using the long fibers, some extended fibers even penetrate through the complete reconstructed volume. Both samples have high porosity (CCM$_{long}$: 63.6%, CCM$_{short}$: 66.8%) and essentially the complete solid phase, as well as the complete pore phase, are interconnected. For CCM$_{long}$, a surface area of 8.2×10^6 m^2/m^3 and for CCM$_{short}$ of 10.6×10^6 m^2/m^3 was calculated, the values being in good agreement with the specific surface area reported for a commercial CCM (Gore PROME A510.1M710.18 C510.4 PEMFC) using a similar FIB-SEM approach.[38]

Figure 7c,d illustrates the pore network of the samples; the blue color represents very small pore channels and the red color larger pore channels up to 160 nm and more, with light blue, green, and yellow colors indicating pore lengths in between these margin values. Both samples have high porosity with a large number of small pores, which are connected by a network of larger pores.

Especially the sample prepared from long fibers shows an increased fraction of large pores. The density of both samples is higher in the region near the membrane (low z-values) than closer to the electrode surface, with the electrode prepared from short fibers being denser than the sample fabricated from long fibers. These differences in the pore structure can only be explained by the shape of the support material and the fabrication procedure. The electrodes are sprayed as 40 bilayers in a fast spray layer-by-layer technique; consequently, when long fibers come
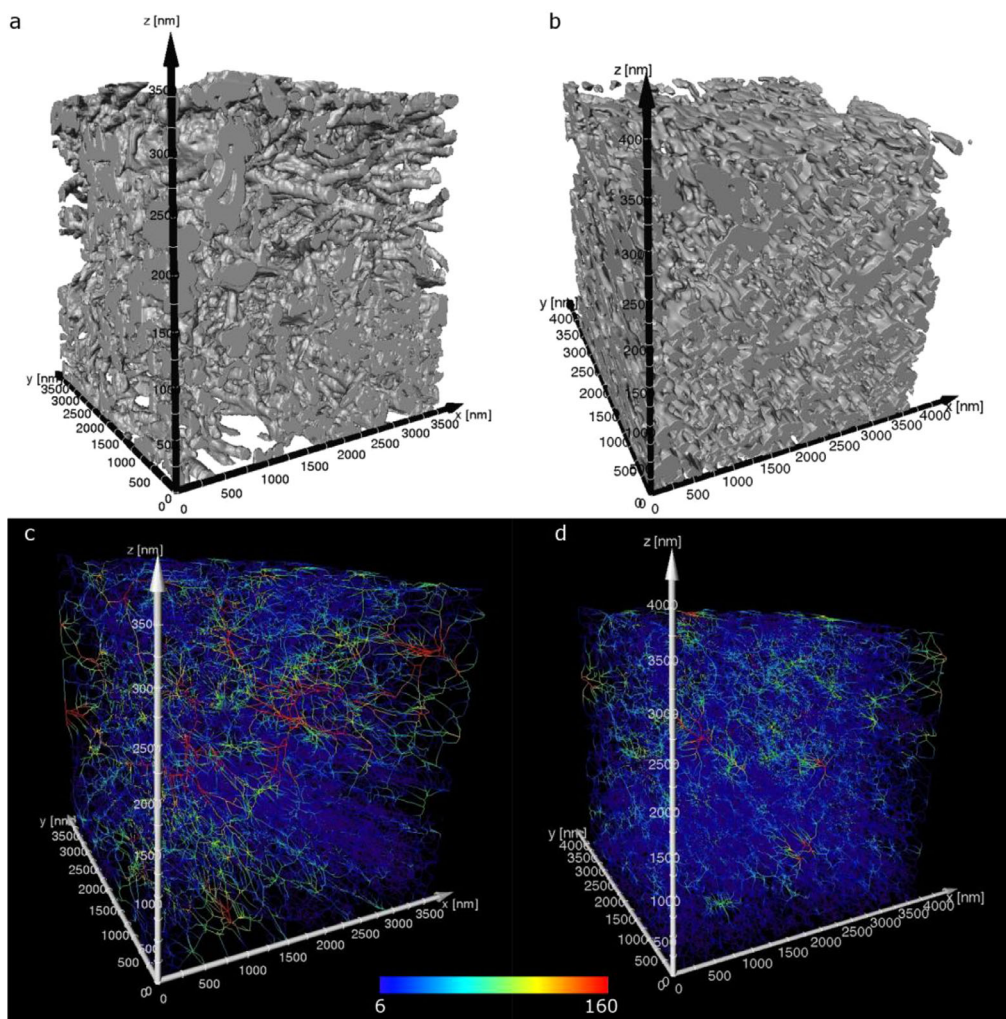
FIGURE 7   3D reconstruction of the cathodes with different support morphologies (a) long fibers, (b) short fibers. (c,d) Illustration of the pore size distribution in both electrodes

down in an area where long fibers have already settled down before, they are hindered in building up a dense layer. Hence, a porous 3D structure is formed that contains higher amounts of large pores and alongside a reduced material density near the surface, leading to the—rather unintentional—formation of a hierarchical structure.

As a stochastic descriptor of the electrode architecture, the chord length distribution of the pore space of both electrodes is depicted in Figure 8. Both samples show a homogeneous distribution with a sharp increase for small pores. The maximum of the chord length distribution is located at the second interval for both samples (50–100 nm), but the maximum frequency is significantly lower for CCM_{long} (9.3% for CCM_{short} vs 7.1% for CCM_{long}). As predicted from the pore network visualization, CCM_{short} shows more small chords compared to CCM_{long}. In CCM_{short} 23.3% of all chords are shorter than 150 nm, in CCM_{long} only 18.0% of all chords are that small.

The mean value of the calculated chord length distribution for CCM_{short} ($cl_{short, mean} = 414 \pm 348$ nm) is noticeably smaller compared to CCM_{long} ($cl_{long, mean} = 633 \pm 583$ nm). This clearly shows that CCM_{long} is comprised of larger pores than CCM_{short}. The high standard deviation for both samples is due to the comparatively broad size distribution of the pore space. Below 500 nm each interval shows a higher percentage of chord lengths for CCM_{short}; above this value, the percentage of measured chord lengths in CCM_{long} is higher. Also, the longest interface–interface distance (4.8 μm), which was observed in our investigation, was found for the CCM_{long} sample. The longest distance observed in CCM_{short} was 3.4 μm and therefore is nearly one-quarter shorter in comparison. Both samples contain large pores cutting through extended areas of the reconstructed part of the electrode. However, the amount of these large pores is significantly higher in the reconstructed volume of the electrode, which has been prepared
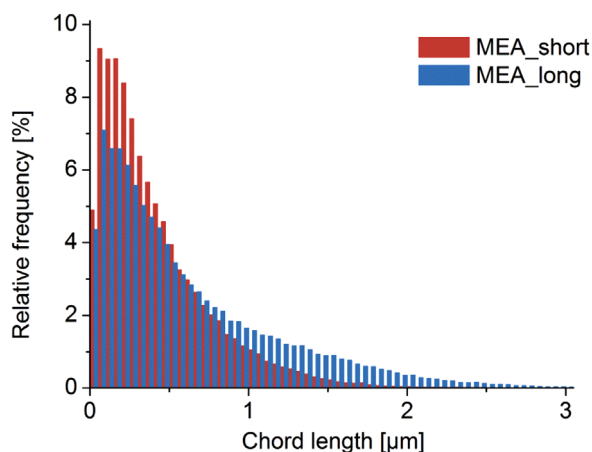
FIGURE 8 Chord length distribution of pore space comparing CCM_{long} with CCM_{short}

from long fibers, than for CCM_{short}. Those large pores presumably facilitate drainage of the reaction product, that is, liquid water, during operation and provide therewith better accessibility of the catalytically active Pt sites for the reactants.

4 | CONCLUSIONS

Three carbon-supported Pt catalysts, differing only in the morphology of their N-doped carbon supports, were prepared by carbonization of differently shaped PANI starting materials and characterized in depth. The chemical identity of the supports with long fiber, short fiber, and granular morphology was confirmed by FTIR, elemental analysis, and Raman spectroscopy. Important to the electrochemical testing, platinum nanoparticle sizes with around 3 nm were verified using XRD and TEM analysis in all cases. Despite the similar chemical identity of the prepared catalysts, different fuel cell performances were obtained, which are the result of the different support morphologies impacting the respective 3D electrode structure of the cathode (porosity, connectivity, and electrode surface area) as analyzed in detail for the CCM with long and short fibers by FIB-SEM investigation and 3D reconstruction. The pore space consists of a significantly higher number of large pores (>500 nm) for CCM_{long}, which was also corroborated by the chord length distribution analysis. Furthermore, the electrode structure appears to be less dense close to the membrane, as long fibers already settled down hinder the incoming ones from building up a close-packed layer. We assume that this structure with a higher number of large pores (and unintentionally hierarchical arrangement) is favorable for reactant flow and water management.

CONFLICT OF INTEREST

The authors declare that they have no conflict of interest.

DATA AVAILABILITY STATEMENT

Data is available on request from the authors.

ORCID

Julia Melke https://orcid.org/0000-0001-5574-0207

REFERENCES

1. R. O'Hayre, D. M. Barnett, F. B. Prinz, The triple phase boundary. *J. Electrochem. Soc.* **2005**, *152*, A439. https://doi.org/10.1149/1.1851054.
2. S. Litster, G. McLean, PEM fuel cell electrodes. *J. Power Sources.* **2004**, *130*, 61–76. https://doi.org/10.1016/j.jpowsour.2003.12.055.
3. M. Bron, C. Roth, Carbon materials in low-temperature polymer electrolyte membrane fuel cells, In: R. C. Alkire, P. N. Bartlett, J. Lipkowski (Eds.), *Electrochem. Carbon Electrodes*, Wiley, **2015**: pp. 241–284. https://doi.org/10.1002/9783527697489.ch7.
4. G. Inoue, K. Yokoyama, J. Ooyama, T. Terao, T. Tokunaga, N. Kubo, M. Kawase, Theoretical examination of effective oxygen diffusion coefficient and electrical conductivity of polymer electrolyte fuel cell porous components, *J. Power Sources.* **2016**, *327*, 610–621. https://doi.org/10.1016/j.jpowsour.2016.07.107.
5. G. Inoue, M. Kawase, Effect of porous structure of catalyst layer on effective oxygen diffusion coefficient in polymer electrolyte fuel cell, *J. Power Sources.* **2016**, *327*, 1–10. https://doi.org/10.1016/j.jpowsour.2016.07.037.
6. B. Millington, V. Whipple, B. G. Pollet, A novel method for preparing proton exchange membrane fuel cell electrodes by the ultrasonic-spray technique, *J. Power Sources.* **2011**, *196*, 8500–8508. https://doi.org/10.1016/j.jpowsour.2011.06.024.
7. R. Liu, W. Zhou, L. Wan, P. Zhang, S. Li, Y. Gao, D. Xu, C. Zheng, M. Shang, Electrostatic spraying of membrane electrode for proton exchange membrane fuel cell, *Curr. Appl. Phys.* **2020**, *20* 11–17. https://doi.org/10.1016/j.cap.2019.09.016.
8. A. B. Andrade, M. L. Mora Bejarano, E. F. Cunha, E. Robalinho, M. Linardi, Fabrication of high precision PEMFC membrane electrode assemblies by sieve printing method, *J. Fuel Cell Sci. Technol.* **2009**, *6*, 0213051–0213053. https://doi.org/10.1115/1.3080556.
9. K. Waldrop, R. Wycisk, P. N. Pintauro, Application of electrospinning for the fabrication of proton-exchange membrane fuel cell electrodes, *Curr. Opin. Electrochem.* **2020**, *21*, 257–264. https://doi.org/10.1016/j.coelec.2020.03.007.
10. M. K. Kayarkatte, Ö. Delikaya, C. Roth, Freestanding catalyst layers: A novel electrode fabrication technique for PEM fuel cells via electrospinning. *ChemElectroChem.* **2017**, *4*, 404–411. https://doi.org/10.1002/celc.201600530.

11. Z. Taie, X. Peng, D. Kulkarni, I. V. Zenyuk, A. Z. Weber, C. Hagen, N. Danilovic, Pathway to complete energy sector decarbonization with available iridium resources using ultralow loaded water electrolyzers. *ACS Appl. Mater. Interfaces.* **2020**, *12*, 52701–52712. https://doi.org/10.1021/acsami.0c15687.

12. Z. Liu, Y. K. Chen-Wiegart, J. Wang, S. A. Barnett, K. T. Faber, Three-Phase 3D reconstruction of a LiCoO$_2$ cathode via FIB-SEM tomography, *Microsc. Microanal.* **2016**, *22*, 140–148. https://doi.org/10.1017/S1431927615015640.

13. A. Chen, J. Bourne, K. Siebein, J. Smith, R. DeHoff, E. Wachsman, K. Jones, FIB characterization of the cathode microstructure in a single solid oxide fuel cell (SOFC), *Microsc. Microanal.* **2007**, *13*, 1504–1505. https://doi.org/10.1017/s1431927607072972.

14. J. S. Hammond, G. L. Fisher, S. R. Bryan, R. Kanarbik, P. Moller, FIB-TOF tomography of solid oxide fuel cells. *Microsc. Microanal.* **2013**, *19*, 672–673. https://doi.org/10.1017/s1431927613005357.

15. K. B. Hatzell, M. B. Dixit, S. A. Berlinger, A. Z. Weber, Understanding inks for porous-electrode formation, *J. Mater. Chem. A.* **2017**, *5*, 20527–20533. https://doi.org/10.1039/c7ta07255d.

16. C. Netzeband, T. Arlt, K. Wippermann, W. Lehnert, I. Manke, Three-dimensional multiscale analysis of degradation of nano- and micro-structure in direct methanol fuel cell electrodes after methanol starvation. *J. Power Sources.* **2016**, *327*, 481–487. https://doi.org/10.1016/j.jpowsour.2016.07.094.

17. Y. Katayanagi, T. Shimizu, Y. Hashimasa, N. Matsushita, Y. Yamazaki, T. Yamaguchi, Cross-sectional observation of nanostructured catalyst layer of polymer electrolyte fuel cell using FIB/SEM. *J. Power Sources.* **2015**, *280*, 210–216. https://doi.org/10.1016/j.jpowsour.2015.01.085.

18. S. Zils, M. Timpel, T. Arlt, A. Wolz, I. Manke, C. Roth, 3D visualisation of PEMFC electrode structures using FIB nanotomography, *Fuel Cells.* **2010**, *10*, 966–972. https://doi.org/10.1002/fuce.201000133.

19. J. Suffner, S. Kaserer, H. Hahn, C. Roth, F. Ettingshausen, Sb-Doped SnO2 hollow spheres offering micro- and nanoporosity in fuel cell electrode structures, *Adv. Energy Mater.* **2011**, *1*, 648–654. https://doi.org/10.1002/aenm.201100077.

20. Z. Fang, M. S. Lee, J. Y. Kim, J. H. Kim, T. F. Fuller, The effect of carbon support surface functionalization on PEM fuel cell performance, durability, and ionomer coverage in the catalyst layer. *J. Electrochem. Soc.* **2020**, *167*, 064506. https://doi.org/10.1149/1945-7111/ab7ea3.

21. Y. C. Park, H. Tokiwa, K. Kakinuma, M. Watanabe, M. Uchida, Effects of carbon supports on Pt distribution, ionomer coverage and cathode performance for polymer electrolyte fuel cells. *J. Power Sources.* **2016**, *315*, 179–191. https://doi.org/10.1016/j.jpowsour.2016.02.091.

22. C. Prado-Burguete, A. Linares-Solano, F. Rodríguez-Reinoso, C. S. M. de Lecea, The effect of oxygen surface groups of the support on platinum dispersion in Pt/carbon catalysts, *J. Catal.* **1989**, *115*, 98–106. https://doi.org/10.1016/0021-9517(89)90010-9.

23. T. Jurzinsky, E. D. Gomez-Villa, M. Kübler, M. Bruns, P. Elsässer, J. Melke, F. Scheiba, C. Cremers, Functionalization of multi-walled carbon nanotubes with indazole. *Electrochim. Acta.* **2019**, *298*, 884–892. https://linkinghub.elsevier.com/retrieve/pii/S0013468618328573 (accessed January 28, 2019).

24. J. Stejskal, I. Sapurina, M. Trchová, Polyaniline nanostructures and the role of aniline oligomers in their formation, *Prog. Polym. Sci.* **2010**, *35*, 1420–1481. https://doi.org/10.1016/j.progpolymsci.2010.07.006.

25. M. Trchová, E. N. Konyushenko, J. Stejskal, J. Kovářová, G. Ćirić-Marjanović, The conversion of polyaniline nanotubes to nitrogen-containing carbon nanotubes and their comparison with multi-walled carbon nanotubes. *Polym. Degrad. Stab.* **2009**, *94*, 929–938. https://doi.org/10.1016/j.polymdegradstab.2009.03.001.

26. S. Mentus, G. Ćirić-Marjanović, M. Trchová, J. Stejskal, Conducting carbonized polyaniline nanotubes, *Nanotechnology.* **2009**, *20*, 245601. https://doi.org/10.1088/0957-4484/20/24/245601.

27. B. Peter, J. Melke, F. Muench, W. Ensinger, C. Roth, Stable platinum nanostructures on nitrogen-doped carbon obtained by high-temperature synthesis for use in PEMFC, *J. Appl. Electrochem.*, **2014**, 1–8.

28. J. Melke, B. Peter, A. Habereder, J. Ziegler, C. Fasel, A. Nefedov, H. Sezen, C. Wöll, H. Ehrenberg, C. Roth, Metal-Support Interactions of Platinum Nanoparticles Decorated N-Doped Carbon Nanofibers for the Oxygen Reduction Reaction, *ACS Appl. Mater. Interfaces.* **2016**, *8*, 82–90. https://doi.org/10.1021/acsami.5b06225.

29. S. Guo, S. Dong, E. Wang, Polyaniline/Pt Hybrid Nanofibers: High-Efficiency Nanoelectrocatalysts for Electrochemical Devices, *Small.* **2009**, *5*, 1869–1876. https://doi.org/10.1002/smll.200900190.

30. E. N. Konyushenko, J. Stejskal, I. Šeděnková, M. Trchová, I. Sapurina, M. Cieslar, J. Prokeš, Polyaniline nanotubes: conditions of formation, *Polym. Int.* **2006**, *55*, 31–39. https://doi.org/10.1002/pi.1899.

31. J. Rodríguez-Carvajal, Recent advances in magnetic structure determination by neutron powder diffraction. *Phys. B Phys. Condens. Matter.* **1993**, *192*, 55–69. https://doi.org/10.1016/0921-4526(93)90108-I.

32. A. Wolz, S. Zils, M. Michel, C. Roth, Structured multilayered electrodes of proton/electron conducting polymer for polymer electrolyte membrane fuel cells assembled by spray coating. *J. Power Sources.* **2010**, *195*, 8162–8167. https://doi.org/10.1016/j.jpowsour.2010.06.087.

33. T. R. Farhat, P. T. Hammond, Designing a new generation of proton-exchange membranes using layer-by-layer deposition of polyelectrolytes. *Adv. Funct. Mater.* **2005**, *15*, 945–954. https://doi.org/10.1002/adfm.200400318.

34. D. Stoeckel, C. Kübel, K. Hormann, A. Höltzel, B. M. Smarsly, U. Tallarek, Morphological analysis of disordered macroporous-mesoporous solids based on physical reconstruction by nanoscale tomography. *Langmuir.* **2014**, *30*, 9022–9027. https://doi.org/10.1021/la502381m.

35. G. A. Zickler, B. Smarsly, N. Gierlinger, H. Peterlik, O. Paris, A reconsideration of the relationship between the crystallite size La of carbons determined by X-ray diffraction and Raman spectroscopy, *Carbon N. Y.* **2006**, *44*, 3239–3246. https://doi.org/10.1016/J.CARBON.2006.06.029.

36. J. Melke, J. Martin, M. Bruns, P. Hügenell, A. Schökel, S. Montoya Isaza, F. Fink, P. Elsässer, A. Fischer, Investigating the effect of microstructure and surface functionalization of mesoporous N-doped carbons on V4+/V5+ kinetics, *ACS Appl. Energy Mater.* 11627-11640, **2011**, *3*. https://doi.org/10.1021/acsaem.0c01489.

37. L.C. M. J. Lázaro, *Study and application of Vulcan XC-72 in low temperature fuel cells.* in: Nova Science Publishers, Inc., pp. 41–68 (**2020**). http://www.researchgate.net/publication/259442510_Study_and_application_of_Vulcan_XC-72_in_low_temperature_fuel_cells

38. T. Hutzenlaub, J. Becker, R. Zengerle, S. Thiele, How coarsening the 3D reconstruction of a porous material influences diffusivity and conductivity values, *ECS Electrochem. Lett.* **2013**, *2*, F14. https://doi.org/10.1149/2.006302eel.